Cerebrospinal Fluid Flow within Ventricles and Subarachnoid Space Evaluated by Velocity Selective Spin Labeling MRI

Yihan Wu[1,2], Feng Xu[1,3], Dan Zhu[1,3], Anna Li[1], Kexin Wang[1,2], Qin Qin[1,3], Jiadi Xu[1,3]

1. F.M. Kirby Research Center for Functional Brain Imaging, Kennedy Krieger Research Institute, Baltimore, MD, USA
2. Department of Biomedical Engineering, Johns Hopkins University, Baltimore, MD, USA
3. Russell H. Morgan Department of Radiology and Radiological Science, Johns Hopkins University School of Medicine, Baltimore, MD, USA.

Corresponding Author:

Jiadi Xu, Ph.D.
Kennedy Krieger Institute
Johns Hopkins University School of Medicine
707 N. Broadway
Baltimore, MD, 21205
E-mail: jxu37@jh.edu
Tel: 443-923-9572
Fax: 443-923-9505

Grant support from NIH: P41EB031771, R01HL149742, R01AG080104 and R21AG074978.

Abstract

This study aims to evaluate cerebrospinal fluid (CSF) flow dynamics within ventricles, and the subarachnoid space (SAS) using the velocity selective spin labeling (VSSL) MRI method with Fourier-transform-based velocity selective inversion preparation. The study included healthy volunteers who underwent MRI scanning with specific VSSL parameters optimized for CSF flow quantification. The VSSL sequence was calibrated against phase-contrast MRI (PC-MRI) to ensure accurate flow velocity measurements. The CSF flow patterns observed in the ventricles were consistent with those obtained using 3D amplified MRI and other advanced MRI techniques, verifying the reliability of the VSSL method. The VSSL method successfully measured CSF flow in the SAS along major arteries, including the middle cerebral artery (MCA), anterior cerebral artery (ACA), and posterior cerebral artery (PCA), with an average flow velocity of $0.339 \pm 0.117\ cm/s$. The diffusion component was well suppressed by flow-compensated gradients, enabling comprehensive mapping of the rapid CSF flow pattern in the SAS system and ventricles. The flow pattern in the SAS system closely resembles the recently discovered perivascular subarachnoid space (PVSAS) system. CSF flow around the MCA, PCA, and ACA arteries in the SAS exhibited a weak orientation dependency. CSF flow in the ventricles was also measured, with an average flow velocity of $0.309 \pm 0.116\ cm/s$, and the highest velocity observed along the superior-inferior direction. This study underscores the potential of VSSL MRI as a non-invasive tool for investigating CSF dynamics in both SAS and ventricles.

Key Words:

Cerebrospinal fluid (CSF), Flow, Subarachnoid space (SAS), Velocity selective spin labeling (VSSL), Fourier-transform-based velocity selective inversion (FT-VSI), Phase-contrast MRI (PC-MRI), Perivascular subarachnoid space (PVSAS)

Introduction

Cerebrospinal fluid (CSF) plays a pivotal role in the central nervous system, providing protection against impact, maintaining chemical homeostasis for brain function, clearing metabolic waste, and distributing nutrients. Recent insights into the glymphatic system reveal CSF's critical part in immune surveillance (1-4) and the clearance of amyloid-beta (5-9), with implications for neurodegenerative diseases (10). However, CSF circulation dynamics are not fully deciphered, with traditional models now questioned due to advanced tracer-based imaging techniques (11-13). The interaction of CSF with the brain's interstitial fluid via the glymphatic system, essential for metabolic waste removal and nutrient distribution, is a key focus. Dysfunctions in this system may contribute to pathological conditions like hydrocephalus and cognitive decline.(14) Recent research has revealed that the CSF circulation in the brain is more complex due to the discovery of a new meningeal layer, known as the subarachnoid lymphatic-like membrane (SLYM) in rodents (15). This membrane segregates the subarachnoid space (SAS) into outer and inner layers. Further studies using a CSF tracer (gadobutrol) and MRI have observed antegrade enhancement of the tracer along the large artery trunks (16). The enhancement appeared circumferentially around major arteries, suggesting the presence of a perivascular subarachnoid space (PVSAS). This space allows for direct, antegrade transport of the tracer along arteries and further into the adjacent cerebral cortex. Additionally, changes in periarterial molecular transport within the PVSAS were associated with reduced intracranial pressure-volume reserve capacity, particularly in patients with idiopathic normal pressure hydrocephalus. (16)

A variety of non-invasive MRI techniques have been developed to image CSF flow (17). These include phase-contrast MRI (PC-MRI) (18-20), time-of-flight (TOF) angiography (21), diffusion-weighted MRI (22-24), and intravoxel incoherent motion (IVIM) (25,26), as well as spin-labeling methods (27,28). These approaches have primarily focused on imaging CSF flow in the ventricles, where the peak flow velocity can reach up to 5 cm/s.(29,30) Detecting meaningful flow in the perivascular space (PVS) remains challenging due to the relatively slow flow velocity and limited size. The predominant approach uses a long echo time (TE) and diffusion-weighted MRI sequence to calculate the pseudo-diffusion coefficient of the PVS and SAS around arteries (22,23). However,

this method is difficult to differentiate between CSF diffusion and pulsatile CSF motion. Despite significant efforts dedicated to studying CSF flow in the ventricles and PVS, it remains unclear how CSF is transported within the large cavity of the SAS. The discovery and study of flow dynamics in the PVSAS still rely heavily on the highly invasive intrathecal injection of tracers (16). In theory, PC-MRI-based flow mapping can be used to visualize CSF flow in the SAS. However, most phase-contrast and spin-labeling methods are limited to single-slice imaging. When aiming to selectively and noninvasively visualize the whole SAS system, the 3D imaging method is still preferred.

Velocity selective spin labeling (VSSL) has utilized the Fourier-transform-based velocity selective pulse train for labeling slow flow while also suppressing the imbalanced diffusion attenuation by using a flow-compensated control (31,32). Fourier-transform-based VSSL pulse trains were designed by concatenating a series of small flip-angle RF pulses, interleaved with paired refocusing pulses and velocity-encoding gradients. These advanced VSSL pulse trains have been effectively employed in different MRI sequences for magnetic resonance angiography (MRA) (33-39), quantitative mapping of blood flow (31,40-48) and blood volume (32,49-51), as well as venous oxygenation (52).

The objective of this work is to propose a non-invasive VSSL MRI technique to selectively visualize and evaluate CSF flow dynamics within the SAS and ventricular systems,. We will fine-tune the VSSL module specifically for CSF flow quantification. Calibration of the flow velocity will be conducted via PC-MRI, and a detailed examination of the flow direction in both the PVSAS and ventricles is planned. This quantitative method provides a novel tool for understanding CSF dynamics in brain development as a promising diagnostic marker candidate for diseases.

Methods

Participants

A total of 14 healthy volunteers (age: 39±17 years; 6 females, 8 males) participated, and the specific number of participants for each study is detailed below. Scanning procedures were conducted on a Philips MR Ingenia Elition 3.0T scanner (Philips Healthcare, Best, The Netherlands), utilizing a quadrature body transmit coil and a 32-channel receive head coil. Ethical approval was obtained from the Johns Hopkins Medicine

Institutional Review Board (IRB), and all participants have provided their informed consent.

VSSL sequence

VSSL pulse train was used in this study, consisting of 9 excitation pulses (20° hard pulses), interleaved with pairs of refocusing pulses (180° composite pulses) and triangular gradient lobes of alternating polarity with 8 velocity-encoding steps (Figure 1A) (31). The control modules used a velocity-compensated gradient configuration for a more balanced diffusion-weighting effect ($b_{label} = 3.57\ s/mm^2, b_{control} = 1.36\ s/mm^2$)(53). Images were then acquired following a post-labeling delay (PLD) of 10 ms to minimize the possible exchange of labeled blood water with CSF.

A 3D-gradient and spin echo (3D-GRASE) readout with linear order was used for image acquisition. The MRI signals from the parenchyma and blood are attenuated by a long TE, taking advantage of their much shorter T_2 relaxation times (<100 ms) than that of CSF (>1000 ms) (54). The imaging parameters were as follows: field of view = 220×165×160 mm^3; slice number 80; acquisition matrix 112×82; reconstruction matrix size 224×224; acquisition resolution = 2×2×2 mm^3; turbo spin echo (TSE) factor = 41 with linear ordering; echo-planar imaging (EPI) factor = 41; SENSE factor (S direction) = 2; echo spacing = 40 ms; TR/effective TE = 10 s/816 ms. An alternative 3D-GRASE readout changing to centric order and effective TE = 39 ms was also evaluated for comparison. We used two-sample t-tests to test whether there is a significant difference between the signal acquired from TE = 816 and 39 ms.

The control and label experiments were repeated six times for averaging, with a total scan duration of 5 minutes for each of the three orthogonal velocity-encoding directions (S-I: superior-inferior; A-P: anterior-posterior; L-R: left-right). M0 image was acquired without VSSL labeling and a TR of 20 s to ensure full recovery of CSF magnetization, other parameters are identical to the VSSL scan.

Simulation

Simulations were performed using MATLAB 2023b (MathWorks, Natick, MA, USA). VSSL module was evaluated through Bloch simulations, including 240-ms duration

with eight 30-ms segments, 16 refocusing pulses (1.74 ms) with MLEV-16 phase cycling, 0.6 ms gradient lobe duration with 0.3 ms ramp time, and maximal gradient strength of 40 mT/m, as illustrated in Figure 1A. The cutoff velocity (V_{cut}) as defined in the VSASL guideline paper (55) was set at 0.29 cm/s. Mz values from label and control were simulated across velocities ranging from −2.0 cm/s to 2.0 cm/s at 0.01 cm/s intervals. In the simulation, a laminar flow model was assumed for simplification. T_1 and T_2 effects were not included in this simulation.

VSSL Optimization for CSF flow

Given that the T_1 and T_2 values of CSF significantly differ from those of brain tissue and blood, the parameters used in MRA and CBF studies are unsuitable for CSF flow mapping. Utilizing a longer T_{seg} reduces the cutoff velocity, which is beneficial for detecting slow CSF flow. However, a longer T_{seg} also prolongs the total duration of the VSSL module, potentially diminishing the overall signal due to T_2 decay. In regions with minimal flow motion, T_2 relaxation becomes the dominant factor, while the VSSL will increase in regions with a wide range of flow rates. Therefore, it is crucial to optimize T_{seg} to maximize the CSF signal, while G_{max} was set to the maximum value of 40 mT/m for the current scanner. Three volunteers (30~56 years old; 2 females, 1 male) have undergone the study of optimizing the VSSL module for CSF imaging. To optimize the VSSL pulse train targeting the CSF flow around arteries, and flow in PVS and ventricles, we varied the duration of each velocity-encoding segment (T_{seg}). We fixed gradient strength (G_{max}) of 40 mT/m, ramp time of 0.3 ms, and a lobe of 0.6 ms, while adjusting T_{seg} as 10, 20, 30, 40, and 50 ms (V_{cut} = 0.86, 0.43, 0.29, 0.21, and 0.17 cm/s, VSSL module duration = 80, 160, 240, 320, 400 ms, respectively).

PVSAS and ventricle assignment

To identify the signal from PVS and ventricles or the CSF flow around the arteries in the SAS, images acquired with VSSL preparation were overlapped with velocity-selective MRA and T_1 weighted (T_{1w}) anatomical images from MPRAGE. MRA was obtained with a Fourier-transform-based velocity selective saturation module followed by a gradient-echo (GRE) readout (56). The VSSL pulse train applied 9 excitation pulses (10°

hard pulses), T_{seg} = 10 ms, G_{max} = 30 mT/m, gradient lobes of 0.6 ms with ramp time of 0.2 ms. MRA scan used identical geometry as those VSSL scans including the field of view, resolution, and orientation. For the GRE readout, resolution = 1×1×1 mm^3, TR/TE = 9.1/1.8 ms, flip angle = 8°, TFE factor = 90 with a centric ordering, and compressed sensing factor = 8 was used. The MPRAGE sequence parameters were as follows: field of view = 220×200×200 mm^3; resolution = 1×1×1 mm^3; TR/TE = 7.9/3.7 ms; TFE factor = 128 with a linear ordering; flip angle = 8°, SENSE factor (P direction) = 2. The total scan duration for MRA and MPRAGE were 1 min and 3.5 min, respectively.

Calibration of the CSF flow measured by VSSL

Eleven volunteers (22~79 years old; 4 females, 7 males) were involved in the calibration study. As demonstrated in Figure 1C, the VSSL signal intensity can be approximated as a linear function of the flow velocity when the flow is slow. Consequently, we calibrated the VSSL-derived velocity maps to actual flow velocity using PC-MRI. The sagittal plane that covers the CA, 4V, and SC was localized using a sagittal MPRAGE scan. Retrospective cardiac-gated 2D phase contrast MRI scans were performed using a 2D single-slice GRE sequence with bipolar velocity-encoding gradients. Each experimental set comprised phase contrast data acquisition at flip angles of 20°, with the remaining MR parameters being a field of view of 220×160 mm^2, an in-plane resolution of 0.5×0.5 mm^2, a slice thickness of 4 mm, TR/TE of 30/20 ms. The velocity encoding (VENC) was set at 10 cm/s across 16 cardiac phases with the flow direction of S-I and at 3 cm/s with the flow direction of A-P and L-R. Physiological waveform monitoring was conducted using a Philips Peripheral Pulse Unit. To correct for background phase offset, all phase images from a cardiac cycle were first averaged to produce a mean phase image. The mean phase image was then processed using a median filter with a 50×50 kernel size. Finally, the filtered mean phase image was subtracted from the phase image of each cardiac phase. (57)

Data analysis

All analyses were processed using custom-written MATLAB scripts. The VSSL images were obtained by subtracting the control and labeled images in a pairwise fashion using a complex subtraction, and subsequently normalized by the M0 signal:

$$I_{VSSL} = Mag[(S_{control} - S_{label})]/Mag[S_{M0}] \quad [1]$$

$S_{control}$, S_{label}, and S_{M0} represent the control, label, and M0 images in complex value, respectively. The $Mag[\cdot]$ operator takes the magnitude of a complex value. I_{S-I}, I_{A-P}, and I_{L-R} represent the normalized VSSL signal acquired with S-I, A-P, and L-R velocity-encoding direction, respectively. ROIs representing CSF within interpeduncular cistern (IPC), prepontine cistern (PPC), and spinal canal (SC) regions were manually delineated on the PC-MRI images to determine flow rates. The VSSL-derived values, extracted using the same ROIs, were correlated with flow velocities obtained from PC-MRI. As VSSL measured the average CSF velocity, the average absolute velocity measured by PC-MRI in one cardiac cycle was used for the calibration.

To access the CSF movement around the arteries in the SAS, we depicted the surroundings of the cerebral arteries shown on MRA. We chose three arteries for the SAS analysis, including M1 and M2 segments of the middle cerebral artery (MCA), A3 segment of the anterior cerebral artery (ACA), P1 and P2 segments of the posterior cerebral artery (PCA). The ventricular ROIs were manually delineated on individual participants' M0 images, including the third ventricle (3V), fourth ventricle (4V), and frontal horn of the lateral ventricle (FLV), cerebral aqueduct (CA), and foramen of Monro (FMo). IPC and SC were also included in our analysis.

To determine whether there are statistically significant differences among the CSF velocities of three orthogonal directions (S-I, A-P, and L-R), we performed a one-way analysis of variance (ANOVA). Following the ANOVA, where a significant F-statistic indicated differences among group means, post-hoc pairwise comparisons were conducted using Tukey's Honest Significant Difference (HSD) test. We considered a *p*-value of less than 0.05 to be statistically significant.

Results

Simulation

Figure 1C illustrates the simulated Mz-velocity responses for the VSSL pulse train with laminar flow integration. At a flow velocity of 0 cm/s (stationary spins), the magnetization is fully inverted by the VSSL pulse train, whereas at flow velocities exceeding 0.29 cm/s, magnetization is partially attenuated (0 to 0.8 of Mz). Below 0.8 cm/s,

the Mz displays a nearly linear relationship with the flow velocity. However, CSF exhibits complex flow patterns in the brain, characterized by a mixture of various orientations and flow velocities, making it challenging to simulate. The simulated Mz-velocity responses for the VSSL pulse train with varying segment times are shown in Supplementary Figure S1 for comparison.

Optimization of T_{seg}

Figure 2 illustrates the T_{seg} optimization of the VSSL pulse train for the CSF flow images. Figure 2A exhibits the VSSL images from a typical subject with varied T_{seg} ranging from 10 ms to 50 ms. The image quality shows an obvious improvement when T_{seg} is increased from 10 ms to 30 ms, as evidenced by the highly reduced background with longer T_{seg}. The background signal may partially originate from the PVS, but this requires further validation. Since the PVS signal is much weaker than the CSF signal in the ventricles and SAS, it is challenging to study and will be addressed in future research. The VSSL signal decays slowly as a function of T_{seg} in most regions. Figure 2B shows the normalized VSSL signal around the MCA, ACA, PCA, and ventricular regions including 4V, CA, and FLV. The signal around MCA and ACA remains relatively stable across T_{seg}. The signal around PCA, 4V, and CA decreases with T_{seg}. Notably, the signal in the FLV, considered as "free-water" with minimal motion (58), decreases from T_{seg} = 10 ms to 30 ms but stabilizes from T_{seg} = 30 ms to 50 ms. The signal in FLV can be used to assess the contribution of the diffusion component. With $T_{/seg}$ = 30 ms, the normalized VSSL signal in FLV is only 0.006, which is far less than (<25%) the normalized VSSL signal around MCA (0.050), ACA (0.028), and PCA (0.070). Thus, T_{seg} = 30 ms was selected for further analysis due to better image quality, low diffusion-weighted effect, and relatively high VSSL signal.

The VSSL signal as a function of TE

Figure 3A presents representative normalized VSSL images acquired at TE of 816 ms and 39 ms for a subject. The velocity-encoding gradient was oriented along the S-I direction. The normalized VSSL signals around the arteries in the SAS and in the ventricles were plotted in Figure 3B and summarized in Table 1. The signals are substantially higher at TE = 39 ms compared to TE = 816 ms, with their signal ratios ranging from 1.14 (CA)

to 2.09 (3V) (Table 1). For the signals around the arteries in SAS, the signal ratios ranged from 1.23 (A3) to 1.91 (P1). Although the normalized VSSL signals at TE = 39 ms are overall higher than those at TE = 816 ms with less T_2-decay effect, significant differences were only found in P1 and P2 segments of the PCA, IPC, and SC, which is expected for CSF with a long T_2 value. When using the VSSL module, a long Tseg (30 ms) was applied, resulting in an extended VSSL preparation time (270 ms), which effectively suppressed both parenchyma and blood signals. The M0 images acquired with a short TE were able to detect weak tissue signal as demonstrated in the Supplementary Figure S2, likely due to the exceptionally long acquisition time, which led to blurring and reduced SNR for the short T_2 components. Despite the enhanced signal at TE = 39 ms, the image quality at TE = 816 ms was superior. The centric ordering used for TE = 39 ms may result in contamination from tissue in the M0 images (Fig. S2).(59) Therefore, we utilized TE = 816 ms for the acquisition.

CSF flow patterns in SAS and ventricles

The CSF flow distribution revealed by the VSSL method is presented in Figure 4. The M0 image is shown in Figure 4A. The images, representing the sum signal of three orthogonal velocity-encoding directions ($I_{sum} = \sqrt{I_{S-I}^2 + I_{A-P}^2 + I_{L-R}^2}$), are depicted in Figures 4B-D. The average of VSSL images acquired from three velocity-encoding directions ($S_{average} = \sum_{S-I,A-P,L-R}(S_{control} - S_{label})\ /3$) is overlaid with the MRA map and the MPRAGE image to identify the arteries in SAS and ventricles (Figures 4E-G). CSF flow around the arteries of M1 and M2 segments of MCA, A3 segment of ACA, and P1 and P2 segments of PCA was detected.

To better visualize the velocity distribution both around the arteries in SAS and in ventricles, maximum-intensity projections (MIP) are shown in Figure 5 with three views. These MIP images were produced directly from the VSSL image $S_{average}$ without any manual enhancement. The VSSL signal in the SAS, especially in the cortical sulci region as demonstrate in the Supplementary Figure S2, is not visible, indicating effective suppression of the diffusion component in the VSSL images (Figure S3). The CSF flow around the arteries of the PCA and MCA is much higher than in other arteries. Rapid CSF flow is mainly observed in the SC and IPC, as well as in ventricles, including the 3V, and

4V. The CSF flow in the CA and FMo is also measured, further validating the VSSL method.

The VSSL method effectively detects CSF flow around the major intracranial arteries (MCA, ACA, and PCA). However, detecting the flow around the basilar artery (BA) is challenging due to the extremely high CSF flow in the PPC, which obscures the CSF flow signal around the BA. The MIP images demonstrate that rapid CSF flow is confined around the MCA, ACA, and PCA, as the signals in the adjacent SAS are relatively low.

Flow velocity calibration with PC-MRI

The CSF movement in the IPC, PPC, and SC were successfully detected using 2D high-resolution PC-MRI in all subjects. Figure 6A illustrates the imaging position of PC-MRI and the detected flow map with VENC of 10 cm/s along the S-I direction from one exemplary subject. The normalized VSSL signal acquired with S-I velocity-encoding direction is plotted in Figure 6B from the same subject for comparison. Figure 6C displays the PC velocity and PC absolute velocity waveform of the ROI shown in Figure 6A for illustration. The pulsatile flow pattern can be clearly visualized. The velocity waveforms were also extracted from all detected ventricles, which showed consistent pulsatile flow patterns across a cardiac cycle. Figure 6D shows the correlation between the normalized VSSL signal and average PC velocity of the whole cardiac cycle values measured by PC-MRI in all three directions, which shows a clear linear correlation. We applied a linear regression model with no intercept term to evaluate the correlation of normalized VSSL signal intensity and PC velocity, and then obtained the velocity maps.

$$V_{VSSL} = (3.65 \pm 0.31) \times I_{VSSL} \quad [2]$$

V_{S-I}, V_{A-P}, and V_{L-R} represent the obtained velocity along S-I, A-P, and L-R direction, respectively. The absolute velocity is calculated by $V_{absolute} = \sqrt{V_{S-I}^2 + V_{A-P}^2 + V_{L-R}^2}$.

The CSF flow along different directions

The typical velocity maps derived from Equation [2] with velocity-encoding gradients along S-I, L-R, and A-P directions and the corresponding boxplots are shown in Figure 7. The VSSL-derived velocities from different ROIs are listed in Table 2. CSF flow around

M1, P1, and P2 exhibit high flow velocities of $0.461 \pm 0.143\ cm/s$. The CSF velocities around M2 and A3 are much slower ($0.155 \pm 0.062\ cm/s$), but the flow velocity is still about 3 times higher than that of the FLV ($0.041 \pm 0.013\ cm/s$). Significant orientation dependence was observed around M2 and A3 ($p < 0.05$), with the highest velocity along the vessel walls. While CSF flow around other arteries also show a consistent trend of the highest velocity along the vessel walls, it does not reach statistical significance. The average CSF flow velocity in ventricles is $0.309 \pm 0.116\ cm/s$. A significantly higher flow velocities along the S-I direction are found in most ventricular regions compared to those of A-P and L-R directions. The CSF flow velocities are $0.525 \pm 0.105\ cm/s$ in IPC and $0.819 \pm 0.157\ cm/s$ in SC.

Discussion

This study proposes the use of the VSSL MRI method to measure the CSF flow velocity within the ventricles and around the arteries in SAS. Modified from the sequence for measuring cerebral blood volume (32,49), the VSSL employed in this CSF study applied Fourier-transform-based inversion instead of Fourier-transform-based saturation pulse trains for higher CSF signals. Both the VSSL pulse train and the 3D-GRASE readout afford extended duration by taking advantage of the rather long CSF T_2 (54). In contrast to previous velocity-selective arterial spin labeling studies which aimed to separate the signal of blood and static tissue into the pass band and stop band of the designed VSSL profiles, this work focuses on the transition band to linearly encode the flow velocity.

The CSF flow pattern observed in the ventricles is highly consistent with those observed using 3D amplified MRI (aMRI) (60) and other MRI methods (29,61). All methods demonstrated that the highest CSF flow occurs around the IPC, SC, and CA regions. The VSSL method can effectively measure CSF flow in the SAS along major arteries, including the MCA, ACA, and PCA. The average CSF flow velocity around the arteries in SAS is $0.339 \pm 0.117\ cm/s$, which is close to and even higher than the flow velocity in the ventricles ($0.309 \pm 0.116\ cm/s$). However, the CSF flow along major veins, such as the superior sagittal sinus, is below the detection threshold of VSSL. Interestingly, there is no clear orientation dependence around most arteries in SAS, except

for the A3 segment of ACA. This suggests that the CSF flow around the arteries in SAS is mainly turbulent. The flow velocity around the proximal arteries in SAS is higher than that of distal arteries, i.e., the velocity around M1 is higher than M2, and P1 is higher than P2 (Figure 7).

It is important to note that many diffusion-based MRI methods have been proposed to analyze CSF dynamics in the PVS (62), such as low b-value dynamic diffusion imaging (24), DTI-ALPS (23), and improved multi-directional diffusion-sensitized driven-equilibrium (iMDDSDE) (61). However, a major challenge in these experiments is suppressing the diffusion component, which can easily be mixed with flow measurements. It is evident in the iMDDSDE study, where signals can be seen in all components filled with CSF such as SAS. The diffusion component is comparable to the flow signal, as evidenced by the dynamic patterns of iMDDSDE over a cardiac cycle. The diffusion component can be separated from the CSF flow by utilizing the fact that flow strongly depends on cardiac movement, which is the principle behind the dynamic diffusion-weighted imaging (dDWI) method. (24) In the current study, we implemented a flow-compensated gradient pair to suppress the diffusion component. The b-value difference between the control and label in VSSL, with the parameters applied in this study, is relatively small ($\Delta b = 2.21\ s\ /\ mm^2$), which is confirmed by the low VSSL signal in the cortex sulci (Fig. S2). In principle, the PVS in penetrating arteries, such as those within the basal ganglia and cortex, can be detected using VSSL with higher b-values and reduced Tseg, as the T_2 in PVS may be significantly shorter than that of CSF in the ventricles. However, the b-value difference between the control and label would be too high to be neglected, requiring an improved b-value compensation approach to effectively suppress the diffusion component. Another key difference between iMDDSDE and VSSL is that the iMDDSDE signal follows a sinusoidal function relative to the flow velocity, making it challenging to distinguish between high and low flow velocities. In contrast, the VSSL signal is still proportional to the flow velocity beyond the V_{cut} as shown in Figure 6D. One more challenge with diffusion-based methods to study CSF flow is that changes in the apparent diffusion coefficient (ADC) can conflate flow changes with variations in perivascular fluid content, capillary perfusion, and even partial volume effect due to

cerebral atrophy (63). The long-TE GRASE technique provides significant advantages by effectively suppressing signals from blood and tissue, which helps to mitigate these issues.

Although a few studies have been conducted specifically on the SAS (64-67), due to the difficulty in suppressing the diffusion component, most research has focused on the entire SAS. With efficient suppression of diffusion and 3D imaging, our study clearly delineates the entire SAS and reveals a pattern of the PVSAS, closely resembling the gadolinium-enhanced imaging results (16). However, whether high CSF flow is confined to the PVSAS or extends to other regions of the SAS requires further investigation. Our method offers a non-invasive tool to examine both the anatomy and CSF dynamics of the SAS system, and has the potential to delineate the newly discovered PVSAS system. Previous research (16) has reported the PVSAS as a donut-shaped form around the arteries, although the exact diameter of the PVSAS was not specified. Based on prior studies of the PVS, normal PVS is generally smaller than 2 mm in size (68). Another study showed that the PVS appears linear when imaged parallel to the course of the vessel, with a diameter generally smaller than 3 mm when imaged perpendicular to the vessel's course (44). Additionally, the VSSL signal around the major arteries in the SAS exceeds 2mm, as demonstrated in Supplementary Figure S3. Thus, we confined our study to the area around the arteries within 1 mm, which aims to mainly focus on the PVSAS system.

PC-MRI exhibits a relatively high noise level, with a mean velocity of 0.45 cm/s measured in the parenchyma. Due to its high baseline noise, PC-MRI faces challenges in accurately measuring low flow rates and is predominantly suitable for regions with high velocities, such as the IPC, PPC, and SC. This limitation significantly restricts PC-MRI's utility in measuring velocities around most arteries in SAS and PVS. Hence, our calibration relies on regions with high velocities, including the IPC, PPC, and SC, assuming a linear correlation between PC-MRI velocity and normalized VSSL signal. Notice that the linear assumption may be only valid for complex flow patterns and may not apply to simpler, single-layer flow. Given the predominance of complex flow in physiological settings, this assumption is valid and is further supported by the PC-MRI calibration study (Figure 6D). With a laminar flow model, the normalized VSSL signal is a linear function of the flow velocity when it is less than 0.8 cm/s.

In this study, we measured the average CSF flow velocity throughout the entire cardiac cycle. Due to the relatively long acquisition times required for the VSSL module and 3D-GRASE readout, it is challenging to measure the velocity waveform within a single cardiac period, as typically done with PC-MRI. While it is still possible to obtain the velocity waveform using a retrospective gating approach similar to that used in the iMDDSDE (61) and dDWI (24) methods, this would significantly increase the total duration of the experiment.

Conclusions

This study successfully employed the VSSL MRI method to measure the CSF flow rate around the arteries in SAS and ventricles. The observed CSF flow patterns in the ventricles were highly consistent with those obtained using 3D amplified MRI (aMRI) and other advanced MRI techniques, verifying the reliability of the VSSL method. The VSSL method demonstrated its capability in measuring CSF flow along major arteries such as the MCA, ACA, and PCA in SAS. Interestingly, the CSF movement along major arteries in SAS showed weak orientation dependence, suggesting a complex driving force for CSF flow. This study underscores the potential of VSSL MRI as a non-invasive tool for investigating CSF dynamics, offering significant insights into the understanding of CSF circulation in both healthy and pathological conditions. Future studies could benefit from the application of improved diffusion compensation approaches to further suppress diffusion components and enhance the accuracy of CSF flow detection in smaller arteries.

Acknowledgments

This work was supported by P41EB031771, R01HL149742, R01AG080104 and R21AG074978. The authors thank D, Mr. Joseph S. Gillen, Mrs. Terri Lee Brawner, Ms. Kathleen A. Kahl, and Ms. Ivana Kusevic for experimental assistance.

References

1. Iliff JJ, Wang M, Liao Y, Plogg BA, Peng W, Gundersen GA, Benveniste H, Vates GE, Deane R, Goldman SA, Nagelhus EA, Nedergaard M. A paravascular pathway facilitates CSF flow through the brain parenchyma and the clearance

of interstitial solutes, including amyloid beta. Sci Transl Med 2012;4(147):147ra111.
2. Iliff JJ, Lee H, Yu M, Feng T, Logan J, Nedergaard M, Benveniste H. Brain-wide pathway for waste clearance captured by contrast-enhanced MRI. J Clin Invest 2013;123(3):1299-1309.
3. Absinta M, Ha SK, Nair G, Sati P, Luciano NJ, Palisoc M, Louveau A, Zaghloul KA, Pittaluga S, Kipnis J, Reich DS. Human and nonhuman primate meninges harbor lymphatic vessels that can be visualized noninvasively by MRI. Elife 2017;6.
4. Ahn JH, Cho H, Kim JH, Kim SH, Ham JS, Park I, Suh SH, Hong SP, Song JH, Hong YK, Jeong Y, Park SH, Koh GY. Meningeal lymphatic vessels at the skull base drain cerebrospinal fluid. Nature 2019;572(7767):62-66.
5. Xu Z, Xiao N, Chen Y, Huang H, Marshall C, Gao J, Cai Z, Wu T, Hu G, Xiao M. Deletion of aquaporin-4 in APP/PS1 mice exacerbates brain Abeta accumulation and memory deficits. Mol Neurodegener 2015;10:58.
6. Xie L, Kang H, Xu Q, Chen MJ, Liao Y, Thiyagarajan M, O'Donnell J, Christensen DJ, Nicholson C, Iliff JJ, Takano T, Deane R, Nedergaard M. Sleep drives metabolite clearance from the adult brain. Science 2013;342(6156):373-377.
7. Rasmussen MK, Mestre H, Nedergaard M. The glymphatic pathway in neurological disorders. The Lancet Neurology 2018;17(11):1016-1024.
8. Louveau A, Da Mesquita S, Kipnis J. Lymphatics in Neurological Disorders: A Neuro-Lympho-Vascular Component of Multiple Sclerosis and Alzheimer's Disease? Neuron 2016;91(5):957-973.
9. Chen X, Liu X, Koundal S, Elkin R, Zhu X, Monte B, Xu F, Dai F, Pedram M, Lee H, Kipnis J, Tannenbaum A, Van Nostrand WE, Benveniste H. Cerebral amyloid angiopathy is associated with glymphatic transport reduction and time-delayed solute drainage along the neck arteries. Nat Aging 2022;2(3):214-223.
10. Da Mesquita S, Louveau A, Vaccari A, Smirnov I, Cornelison RC, Kingsmore KM, Contarino C, Onengut-Gumuscu S, Farber E, Raper D, Viar KE, Powell RD, Baker W, Dabhi N, Bai R, Cao R, Hu S, Rich SS, Munson JM, Lopes MB, Overall CC, Acton ST, Kipnis J. Functional aspects of meningeal lymphatics in ageing and Alzheimer's disease. Nature 2018;560(7717):185-191.
11. Ma Q, Ineichen BV, Detmar M, Proulx ST. Outflow of cerebrospinal fluid is predominantly through lymphatic vessels and is reduced in aged mice. Nat Commun 2017;8(1):1434.
12. Norwood JN, Zhang Q, Card D, Craine A, Ryan TM, Drew PJ. Anatomical basis and physiological role of cerebrospinal fluid transport through the murine cribriform plate. Elife 2019;8.
13. Stanton EH, Persson NDA, Gomolka RS, Lilius T, Sigurethsson B, Lee H, Xavier ALR, Benveniste H, Nedergaard M, Mori Y. Mapping of CSF transport using high spatiotemporal resolution dynamic contrast-enhanced MRI in mice: Effect of anesthesia. Magn Reson Med 2021;85(6):3326-3342.
14. van der Thiel MM, Backes WH, Ramakers IH, Jansen JF. Novel developments in non-contrast enhanced MRI of the perivascular clearance system: What

are the possibilities for Alzheimer's disease research? Neuroscience & Biobehavioral Reviews 2023;144:104999.
15. Mollgard K, Beinlich FRM, Kusk P, Miyakoshi LM, Delle C, Pla V, Hauglund NL, Esmail T, Rasmussen MK, Gomolka RS, Mori Y, Nedergaard M. A mesothelium divides the subarachnoid space into functional compartments. Science 2023;379(6627):84-88.
16. Eide PK, Ringstad G. Functional analysis of the human perivascular subarachnoid space. Nature Communications 2024;15(1).
17. Taoka T, Naganawa S. Glymphatic imaging using MRI. J Magn Reson Imaging 2019.
18. Jaeger M, Khoo AK, Conforti DA, Cuganesan R. Relationship between intracranial pressure and phase contrast cine MRI derived measures of intracranial pulsations in idiopathic normal pressure hydrocephalus. J Clin Neurosci 2016;33:169-172.
19. Huang TY, Chung HW, Chen MY, Giiang LH, Chin SC, Lee CS, Chen CY, Liu YJ. Supratentorial cerebrospinal fluid production rate in healthy adults: quantification with two-dimensional cine phase-contrast MR imaging with high temporal and spatial resolution. Radiology 2004;233(2):603-608.
20. Sakhare AR, Barisano G, Pa J. Assessing test-retest reliability of phase contrast MRI for measuring cerebrospinal fluid and cerebral blood flow dynamics. Magn Reson Med 2019;82(2):658-670.
21. Kuo PH, Stuehm C, Squire S, Johnson K. Meningeal Lymphatic Vessel Flow Runs Countercurrent to Venous Flow in the Superior Sagittal Sinus of the Human Brain. Tomography 2018;4(3):99-104.
22. Harrison IF, Siow B, Akilo AB, Evans PG, Ismail O, Ohene Y, Nahavandi P, Thomas DL, Lythgoe MF, Wells JA. Non-invasive imaging of CSF-mediated brain clearance pathways via assessment of perivascular fluid movement with diffusion tensor MRI. Elife 2018;7.
23. Taoka T, Masutani Y, Kawai H, Nakane T, Matsuoka K, Yasuno F, Kishimoto T, Naganawa S. Evaluation of glymphatic system activity with the diffusion MR technique: diffusion tensor image analysis along the perivascular space (DTI-ALPS) in Alzheimer's disease cases. Jpn J Radiol 2017;35(4):172-178.
24. Wen Q, Tong Y, Zhou X, Dzemidzic M, Ho CY, Wu YC. Assessing pulsatile waveforms of paravascular cerebrospinal fluid dynamics within the glymphatic pathways using dynamic diffusion-weighted imaging (dDWI). Neuroimage 2022;260:119464.
25. Taoka T, Kawai H, Nakane T, Abe T, Nakamichi R, Ito R, Sato Y, Sakai M, Naganawa S. Diffusion analysis of fluid dynamics with incremental strength of motion proving gradient (DANDYISM) to evaluate cerebrospinal fluid dynamics. Jpn J Radiol 2021;39(4):315-323.
26. Becker AS, Boss A, Klarhoefer M, Finkenstaedt T, Wurnig MC, Rossi C. Investigation of the pulsatility of cerebrospinal fluid using cardiac-gated Intravoxel Incoherent Motion imaging. Neuroimage 2018;169:126-133.
27. Yamada S, Miyazaki M, Kanazawa H, Higashi M, Morohoshi Y, Bluml S, McComb JG. Visualization of cerebrospinal fluid movement with spin labeling

at MR imaging: preliminary results in normal and pathophysiologic conditions. Radiology 2008;249(2):644-652.
28. Yamada S, Miyazaki M, Yamashita Y, Ouyang C, Yui M, Nakahashi M, Shimizu S, Aoki I, Morohoshi Y, McComb JG. Influence of respiration on cerebrospinal fluid movement using magnetic resonance spin labeling. Fluids Barriers CNS 2013;10(1):36.
29. Stadlbauer A, Salomonowitz E, Van Der Riet W, Buchfelder M, Ganslandt O. Insight into the patterns of cerebrospinal fluid flow in the human ventricular system using MR velocity mapping. Neuroimage 2010;51(1):42-52.
30. Yamada S, Ishikawa M, Ito H, Yamamoto K, Yamaguchi M, Oshima M, Nozaki K. Cerebrospinal fluid dynamics in idiopathic normal pressure hydrocephalus on four-dimensional flow imaging. European radiology 2020;30:4454-4465.
31. Qin Q, van Zijl PC. Velocity-selective-inversion prepared arterial spin labeling. Magnetic resonance in medicine 2016;76(4):1136-1148.
32. Qin Q, Qu Y, Li W, Liu D, Shin T, Zhao Y, Lin DD, van Zijl PC, Wen Z. Cerebral blood volume mapping using Fourier-transform–based velocity-selective saturation pulse trains. Magnetic resonance in medicine 2019;81(6):3544-3554.
33. Qin Q, Shin T, Schär M, Guo H, Chen H, Qiao Y. Velocity-selective magnetization-prepared non-contrast-enhanced cerebral MR angiography at 3 Tesla: improved immunity to B0/B1 inhomogeneity. Magnetic resonance in medicine 2016;75(3):1232-1241.
34. Shin T, Qin Q, Park JY, Crawford RS, Rajagopalan S. Identification and reduction of image artifacts in non–contrast-enhanced velocity-selective peripheral angiography at 3T. Magnetic resonance in medicine 2016;76(2):466-477.
35. Li W, Xu F, Schär M, Liu J, Shin T, Zhao Y, van Zijl PC, Wasserman BA, Qiao Y, Qin Q. Whole-brain arteriography and venography: using improved velocity-selective saturation pulse trains. Magnetic resonance in medicine 2018;79(4):2014-2023.
36. Shin T, Qin Q. Characterization and suppression of stripe artifact in velocity-selective magnetization-prepared unenhanced MR angiography. Magnetic resonance in medicine 2018;80(5):1997-2005.
37. Zhu D, Li W, Liu D, Liu G, Pei Y, Shin T, Sedaghat F, Qin Q. Non-contrast-enhanced abdominal MRA at 3 T using velocity-selective pulse trains. Magnetic resonance in medicine 2020;84(3):1173-1183.
38. Xu F, Zhu D, Fan H, Lu H, Liu D, Li W, Qin Q. Magnetic resonance angiography and perfusion mapping by arterial spin labeling using Fourier transform–based velocity-selective pulse trains: examination on a commercial perfusion phantom. Magnetic resonance in medicine 2021;86(3):1360-1368.
39. Liu D, Zhu D, Qin Q. Direct angiographic comparison of different velocity-selective saturation, inversion, and DANTE labeling modules on cerebral arteries. Magnetic resonance in medicine 2024.
40. Landes V, Javed A, Jao T, Qin Q, Nayak K. Improved velocity-selective labeling pulses for myocardial ASL. Magnetic resonance in medicine 2020;84(4):1909-1918.

41. Liu D, Xu F, Li W, van Zijl PC, Lin DD, Qin Q. Improved velocity-selective-inversion arterial spin labeling for cerebral blood flow mapping with 3D acquisition. Magnetic resonance in medicine 2020;84(5):2512-2522.
42. Franklin SL, Bones IK, Harteveld AA, Hirschler L, van Stralen M, Qin Q, de Boer A, Hoogduin JM, Bos C, van Osch MJ. Multi-organ comparison of flow-based arterial spin labeling techniques: spatially non-selective labeling for cerebral and renal perfusion imaging. Magnetic resonance in medicine 2021;85(5):2580-2594.
43. Liu D, Li W, Xu F, Zhu D, Shin T, Qin Q. Ensuring both velocity and spatial responses robust to field inhomogeneities for velocity-selective arterial spin labeling through dynamic phase-cycling. Magnetic resonance in medicine 2021;85(5):2723-2734.
44. Liu D, Jiang D, Tekes A, Kulikowicz E, Martin LJ, Lee JK, Liu P, Qin Q. Multi-parametric evaluation of cerebral hemodynamics in neonatal piglets using non-contrast-enhanced magnetic resonance imaging methods. Journal of Magnetic Resonance Imaging 2021;54(4):1053-1065.
45. Qu Y, Kong D, Wen H, Ou X, Rui Q, Wang X, Lin DD, Qin Q, Wen Z. Perfusion measurement in brain gliomas using velocity-selective arterial spin labeling: comparison with pseudo-continuous arterial spin labeling and dynamic susceptibility contrast MRI. European radiology 2022;32(5):2976-2987.
46. Xu F, Liu D, Zhu D, Hillis AE, Bakker A, Soldan A, Albert MS, Lin DD, Qin Q. Test-retest reliability of 3D velocity-selective arterial spin labeling for detecting normal variations of cerebral blood flow. Neuroimage 2023;271:120039.
47. Lambrecht S, Liu D, Dzaye O, Kamson DO, Reis J, Liebig T, Holdhoff M, Van Zijl P, Qin Q, Lin DD. Velocity-Selective Arterial Spin Labeling Perfusion in Monitoring High Grade Gliomas Following Therapy: Clinical Feasibility at 1.5 T and Comparison with Dynamic Susceptibility Contrast Perfusion. Brain Sciences 2024;14(2):126.
48. Xu F, Xu C, Zhu D, Liu D, Lu H, Qin Q. Evaluating cerebrovascular reactivity measured by velocity selective inversion arterial spin labeling with different post-labeling delays: The effect of fast flow. Magnetic Resonance in Medicine 2024.
49. Li W, Liu D, van Zijl PC, Qin Q. Three-dimensional whole-brain mapping of cerebral blood volume and venous cerebral blood volume using Fourier transform–based velocity-selective pulse trains. Magnetic resonance in medicine 2021;86(3):1420-1433.
50. Liu D, Zhu D, Xu F, Sedaghat F, Qin Q. Prostate perfusion mapping using Fourier-transform based velocity-selective arterial spin labeling: Choice of cutoff velocity and comparison with brain. Magnetic resonance in medicine 2023;90(3):1121-1129.
51. Zhu D, Xu F, Liu D, Hillis AE, Lin D, van Zijl PC, Qin Q. Evaluation of 3D stack-of-spiral turbo FLASH acquisitions for pseudo-continuous and velocity-selective ASL–derived brain perfusion mapping. Magnetic resonance in medicine 2023;90(3):939-949.

52. Li W, Xu F, Zhu D, van Zijl PC, Qin Q. T2-oximetry–based cerebral venous oxygenation mapping using Fourier-transform–based velocity-selective pulse trains. Magnetic resonance in medicine 2022;88(3):1292-1302.
53. Liu D, Xu F, Lin DD, van Zijl PC, Qin Q. Quantitative measurement of cerebral blood volume using velocity-selective pulse trains. Magnetic resonance in medicine 2017;77(1):92-101.
54. Qin Q. A simple approach for three-dimensional mapping of baseline cerebrospinal fluid volume fraction. Magnetic resonance in medicine 2011;65(2):385-391.
55. Qin Q, Alsop DC, Bolar DS, Hernandez-Garcia L, Meakin J, Liu D, Nayak KS, Schmid S, van Osch MJP, Wong EC, Woods JG, Zaharchuk G, Zhao MY, Zun Z, Guo J, Group ISS. Velocity-selective arterial spin labeling perfusion MRI: A review of the state of the art and recommendations for clinical implementation. Magn Reson Med 2022;88(4):1528-1547.
56. Li W, Xu F, Schar M, Liu J, Shin T, Zhao Y, van Zijl PCM, Wasserman BA, Qiao Y, Qin Q. Whole-brain arteriography and venography: Using improved velocity-selective saturation pulse trains. Magn Reson Med 2017:10.1002/mrm.26864.
57. Tang J, Heidari Pahlavian S, Joe E, Gamez MT, Zhao T, Ma SJ, Jin J, Cen SY, Chui HC, Yan L. Assessment of arterial pulsatility of cerebral perforating arteries using 7T high-resolution dual-VENC phase-contrast MRI. Magnetic Resonance in Medicine 2024;92(2):605-617.
58. Bito Y, Harada K, Ochi H, Kudo K. Low b-value diffusion tensor imaging for measuring pseudorandom flow of cerebrospinal fluid. Magnetic Resonance in Medicine 2021;86(3):1369-1382.
59. Constable R, Anderson A, Zhong J, Gore J. Factors influencing contrast in fast spin-echo MR imaging. Magnetic resonance imaging 1992;10(4):497-511.
60. Terem I, Dang L, Champagne A, Abderezaei J, Pionteck A, Almadan Z, Lydon AM, Kurt M, Scadeng M, Holdsworth SJ. 3D amplified MRI (aMRI). Magn Reson Med 2021;86(3):1674-1686.
61. Ran L, He Y, Zhu J, Long F, Dong Y, Song X, Wang W, Wang M. Characterizing cerebrospinal fluid mobility using heavily T2-weighted 3D fast spin echo (FSE) imaging with improved multi-directional diffusion-sensitized driven-equilibrium (iMDDSDE) preparation. J Cereb Blood Flow Metab 2023;44(1):105-117.
62. Wright AM, Wu YC, Feng L, Wen Q. Diffusion magnetic resonance imaging of cerebrospinal fluid dynamics: Current techniques and future advancements. NMR Biomed 2024.
63. Wright AM, Wu YC, Chen NK, Wen Q. Exploring Radial Asymmetry in MR Diffusion Tensor Imaging and Its Impact on the Interpretation of Glymphatic Mechanisms. J Magn Reson Imaging 2023.
64. Hirschler L, Runderkamp BA, Franklin SL, van Harten T, Nederveen A, Caan M, van Osch M. The driving force of glymphatics: influence of the cardiac cycle on CSF-mobility in perivascular spaces in humans. Proc of the Int Soc of Mag Res in Medicine 2020.

65. Hirschler L, Runderkamp BA, van Veluw SJ, Caan M, van Osch M. Effects of the cardiac and respiratory cycles on CSF-mobility in human subarachnoid and perivascular spaces. 2022. p 7-12.
66. Hu Z, Jiang D, Cao Y, Fan H, Shi W, Lu H. Monitoring pulsatile CSF motion in the subarachnoid space using MRI. In Proceedings of the 32nd Annual Meeting of International Society for Magnetic Resonance in Medicine, Singapore 2024:1186.
67. Harrison IF, Siow B, Akilo AB, Evans PG, Ismail O, Ohene Y, Nahavandi P, Thomas DL, Lythgoe MF, Wells JA. Non-invasive imaging of CSF-mediated brain clearance pathways via assessment of perivascular fluid movement with diffusion tensor MRI. Elife 2018;7:e34028.
68. Barisano G, Lynch KM, Sibilia F, Lan H, Shih N-C, Sepehrband F, Choupan J. Imaging perivascular space structure and function using brain MRI. Neuroimage 2022;257:119329.

Table 1. The normalized VSSL signal, signal ratio, and *p*-value with signal acquired at TE = 816 and 39 ms for each ROI. A two-sample t-test was used to measure whether there is a significant difference between the normalized signals acquired at TE = 816 and 39 ms (N = 3).

ROI	M1	M2	P1	P2	A3	FLV	3V	4V	FMo	CA	IPC	SC
TE = 816 ms	0.051	0.027	0.095	0.067	0.037	0.007	0.048	0.045	0.042	0.164	0.088	0.213
TE = 39 ms	0.072	0.042	0.181	0.104	0.045	0.011	0.099	0.075	0.075	0.187	0.161	0.272
Signal Ratio	1.413	1.521	1.912	1.557	1.225	1.663	2.086	1.642	1.786	1.138	1.824	1.276
p-value	0.080	0.168	0.001	0.023	0.337	0.134	0.155	0.122	0.311	0.662	0.018	0.038

Table 2. Statistical results of VSSL-derived velocity along S-I, L-R, and A-P directions, and absolute velocity (N = 10).

Velocity in ROIs (cm/s)		M1	M2	P1	P2	A3	FLV	3V	4V	FMo	CA	IPC	SC
S-I	Mean	0.208	0.111	0.376	0.215	0.078	0.024	0.221	0.198	0.179	0.572	0.329	0.735
	SD	0.084	0.051	0.106	0.069	0.035	0.008	0.085	0.096	0.072	0.155	0.068	0.150
L-R	Mean	0.281	0.078	0.318	0.191	0.040	0.019	0.081	0.070	0.077	0.147	0.268	0.168
	SD	0.093	0.029	0.112	0.052	0.010	0.005	0.024	0.039	0.042	0.059	0.061	0.053
A-P	Mean	0.222	0.136	0.315	0.240	0.074	0.026	0.240	0.073	0.123	0.386	0.306	0.302
	SD	0.067	0.056	0.128	0.070	0.029	0.014	0.088	0.035	0.064	0.113	0.070	0.102
Absolute Velocity	Mean	0.416	0.194	0.589	0.378	0.116	0.041	0.338	0.224	0.232	0.711	0.525	0.819
	SD	0.135	0.076	0.184	0.096	0.043	0.013	0.120	0.105	0.100	0.178	0.105	0.157

p-value in ROIs		M1	M2	P1	P2	A3	FLV	3V	4V	FMo	CA	IPC	SC
ANOVA		0.123	0.033	0.432	0.251	0.007	0.268	<0.001	<0.001	0.003	<0.001	0.140	<0.001
HSD Test	S-I vs L-R	n.s.	n.s.	n.s.	n.s.	0.012	n.s.	<0.001	<0.001	0.002	<0.001	n.s.	<0.001
	S-I vs A-P	n.s.	n.s.	n.s.	n.s.	n.s.	n.s.	n.s.	<0.001	n.s.	0.003	n.s.	<0.001
	L-R vs A-P	n.s.	0.025	n.s.	n.s.	0.022	n.s.	<0.001	n.s.	n.s.	<0.001	n.s.	0.028

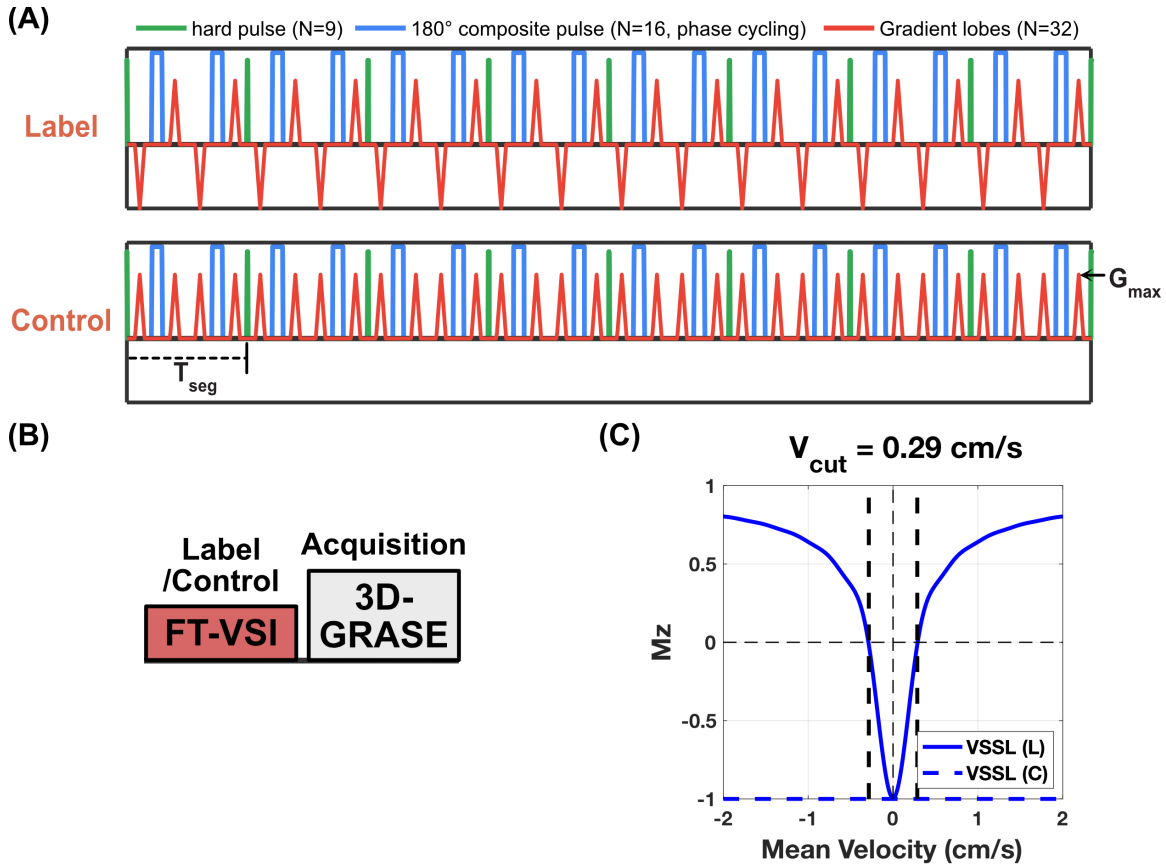

Figure 1. Illustration of the Fourier-transform-based velocity selective inversion pulse train, VSSL sequence, and the VSSL magnetization as a function of mean velocity. (A) Diagram illustrating the Fourier-transform-based velocity selective inversion pulse train, where velocity-selective labeling is employed to mark the flow within CSF. In each velocity-encoding step, a 20° excitation pulse is followed by a pair of refocusing pulses. Gradients with alternating polarity surround the refocusing pulses for the velocity- sensitive waveform (label), and uni-polar gradients are used for the velocity-compensated waveform (control) in the velocity-encoding steps. The segment time (T_{seg}) and maximum gradient (G_{max}) for the flow encoding are labeled in the sequence. (B) Diagram illustrating the VSSL sequence. After the velocity selective inversion pulse train, a post-labeling delay of 10 ms precedes the readout. A 3D-GRASE readout with a long TE is applied to image CSF while attenuating signals from parenchyma and blood. (C) Simulated Mz-velocity responses for the VSSL pulse train. Velocity-sensitive and velocity-compensated profiles are represented by solid and dashed blue lines, respectively. The cut-off velocity (V_{cut}) is delineated at the first intersection where $\Delta M = 1$, highlighted by vertical black dashed lines at a velocity of

0.29 cm/s. Parameters used in the simulation, such as number of segments (8), T_{seg} (30 ms), and G_{max} (40 mT/m), are consistent with those employed in our study.

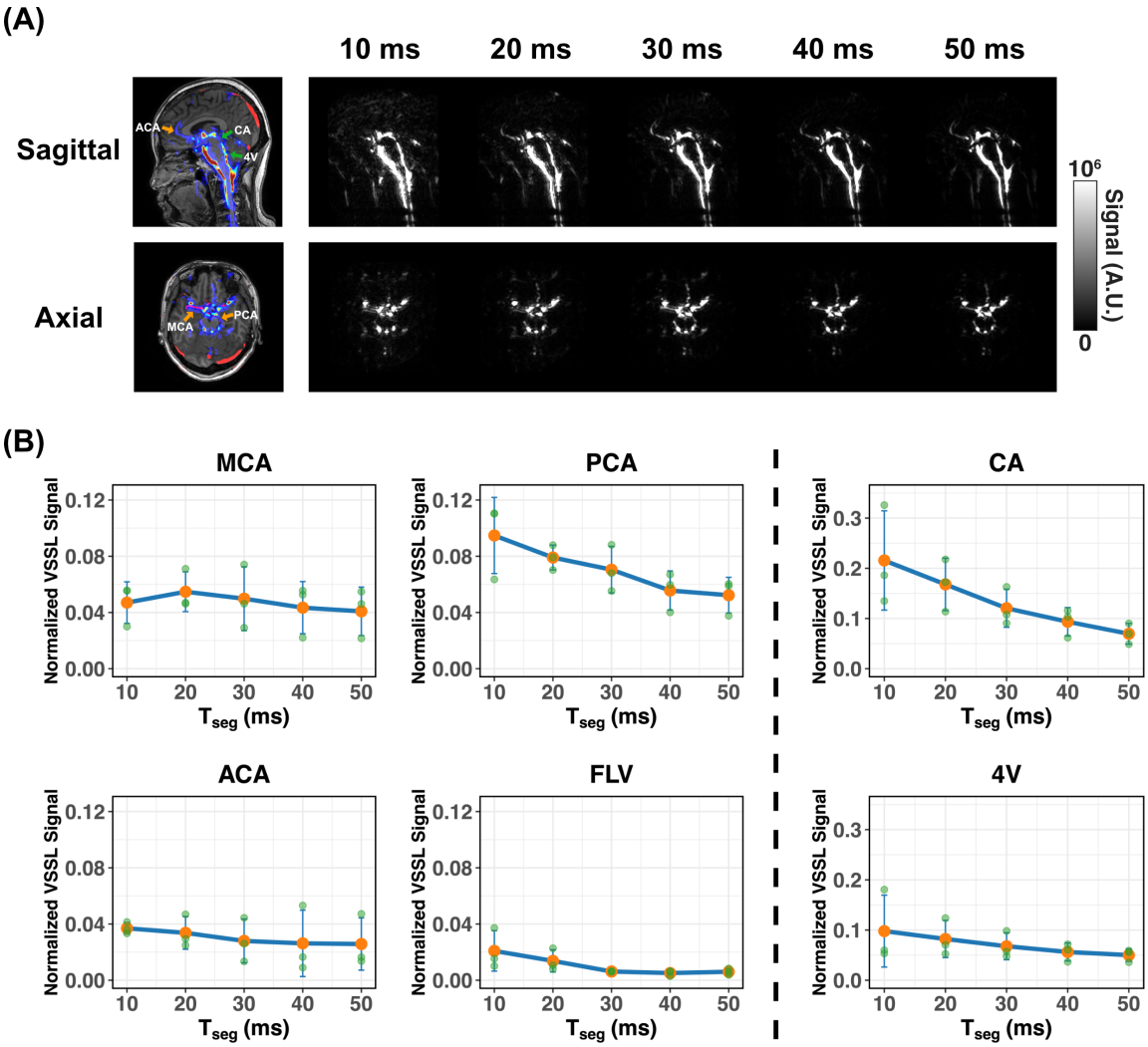

Figure 2. T_{seg} Optimization. (A) Example VSSL images from one subject acquired with different T_{seg} in sagittal and axial views. The left images, overlapped with MRA and MPRAGE images, show the ROIs for the VSSL signal presented below. (B) Normalized VSSL signal as a function of T_{seg} around MCA, ACA, and PCA, as well as at the 4V, CA, and FLV (N = 3, error bars represent standard derivation). The normalized VSSL signal around MCA and ACA are relatively stable across different T_{seg}, while the signal decreased significantly from T_{seg} = 10 to 30 ms in the CA, 4V, FLV, and around PCA. The arteries in SAS are indicated with yellow arrows, and other ROIs are labeled with green arrows.

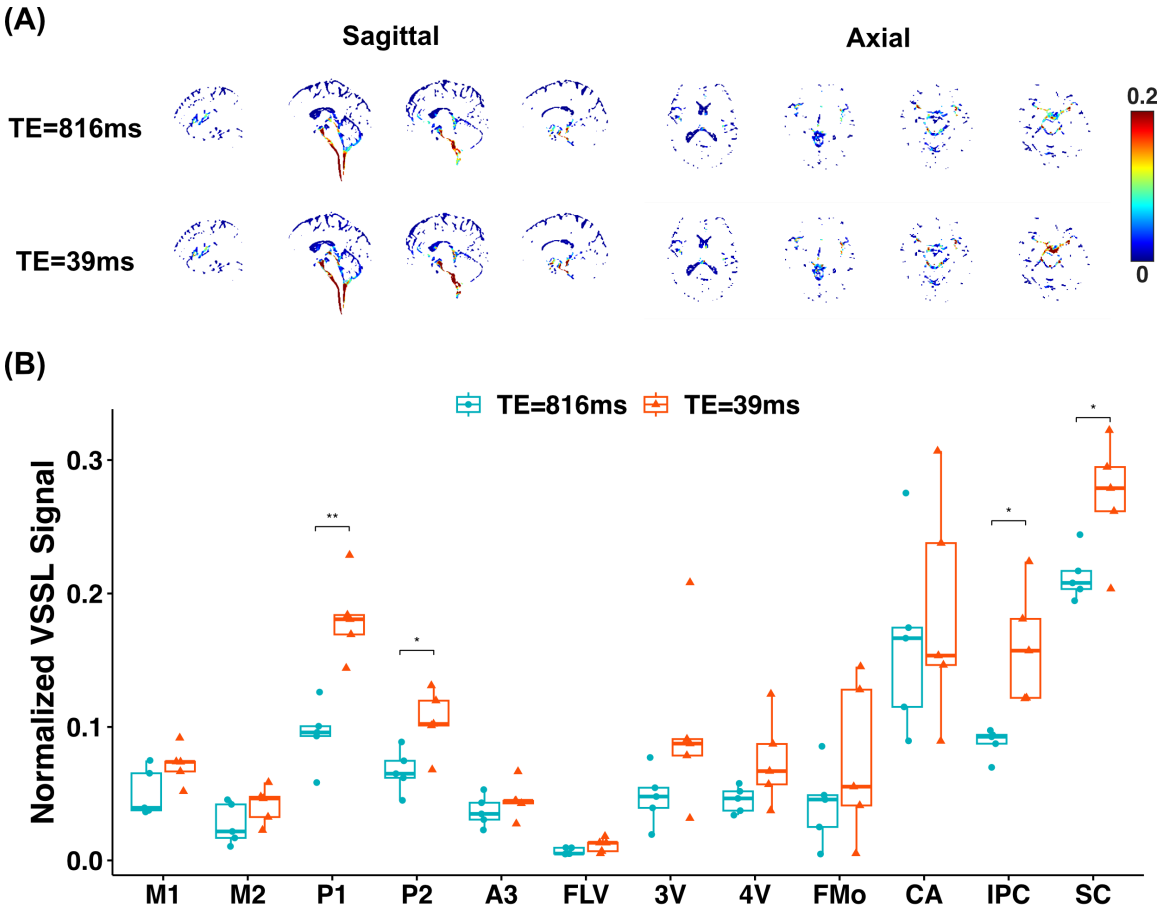

Figure 3. The results for the normalized VSSL signal with different TEs. (A) The typical normalized VSSL images acquired at TE = 816 and 39 ms with S-I velocity-encoding gradient directions for a representative healthy subject. (B) The boxplot of normalized VSSL signals in each ROI with different TE. A two-sample t-test was performed for comparison (* $p < 0.05$, ** $p < 0.01$).

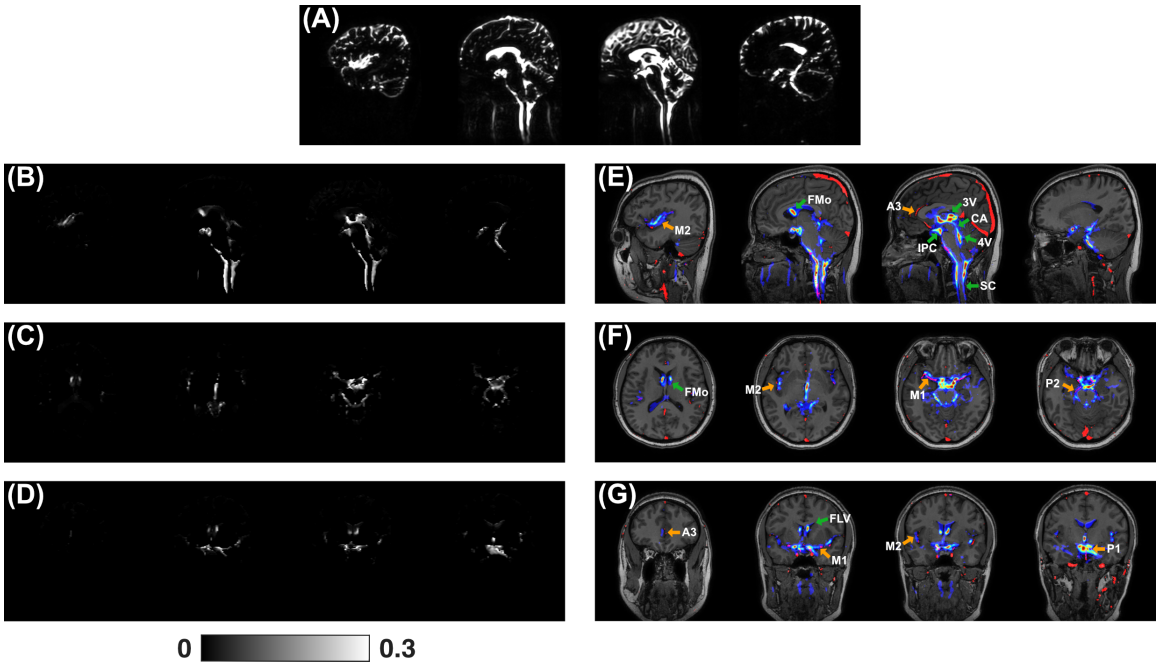

Figure 4. The M0 map (A) and normalized VSSL images (I_{sum}) in sagittal (B), axial (C), and coronal (D) views. VSSL images were acquired with T_{seg} = 30 ms and G_{max} = 40 mT/m. VSSL image ($S_{average}$) was overlaid with the MRA map and MPRAGE image in sagittal (E), axial (F), and coronal (G) views. The MRA map is shown in red, and the unnormalized VSSL signal is displayed using a jet colormap. The arteries in SAS are indicated with yellow arrows, and other ROIs are labeled with green arrows.

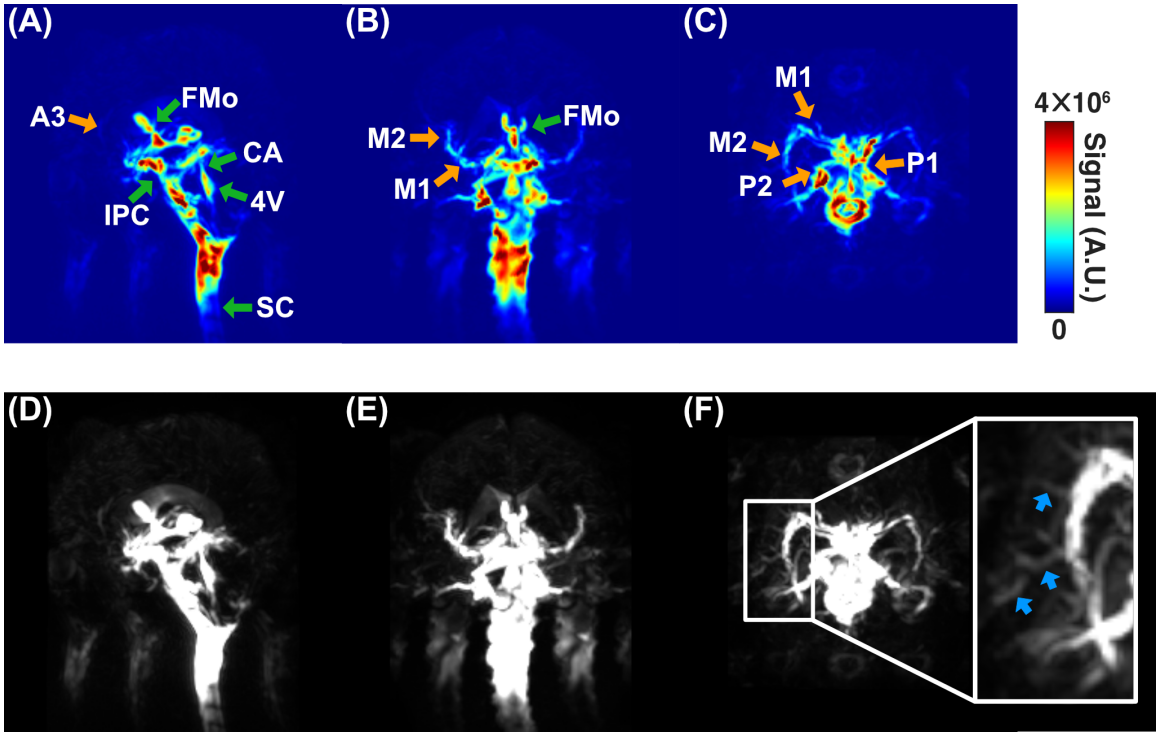

Figure 5. Maximum-Intensity Projections (MIP) of the VSSL image ($S_{average}$) in sagittal (A, D), coronal (B, E), and axial (C, F) views. The top row images (A-C) use a jet colormap to show the VSSL signal in the SAS and ventricles. The bottom row images (D-F) employ a zoomed scale to highlight the small arteries, as shown by blue arrows in the inset figure. The arteries in SAS are indicated with yellow arrows, and other ROIs are labeled with green arrows.

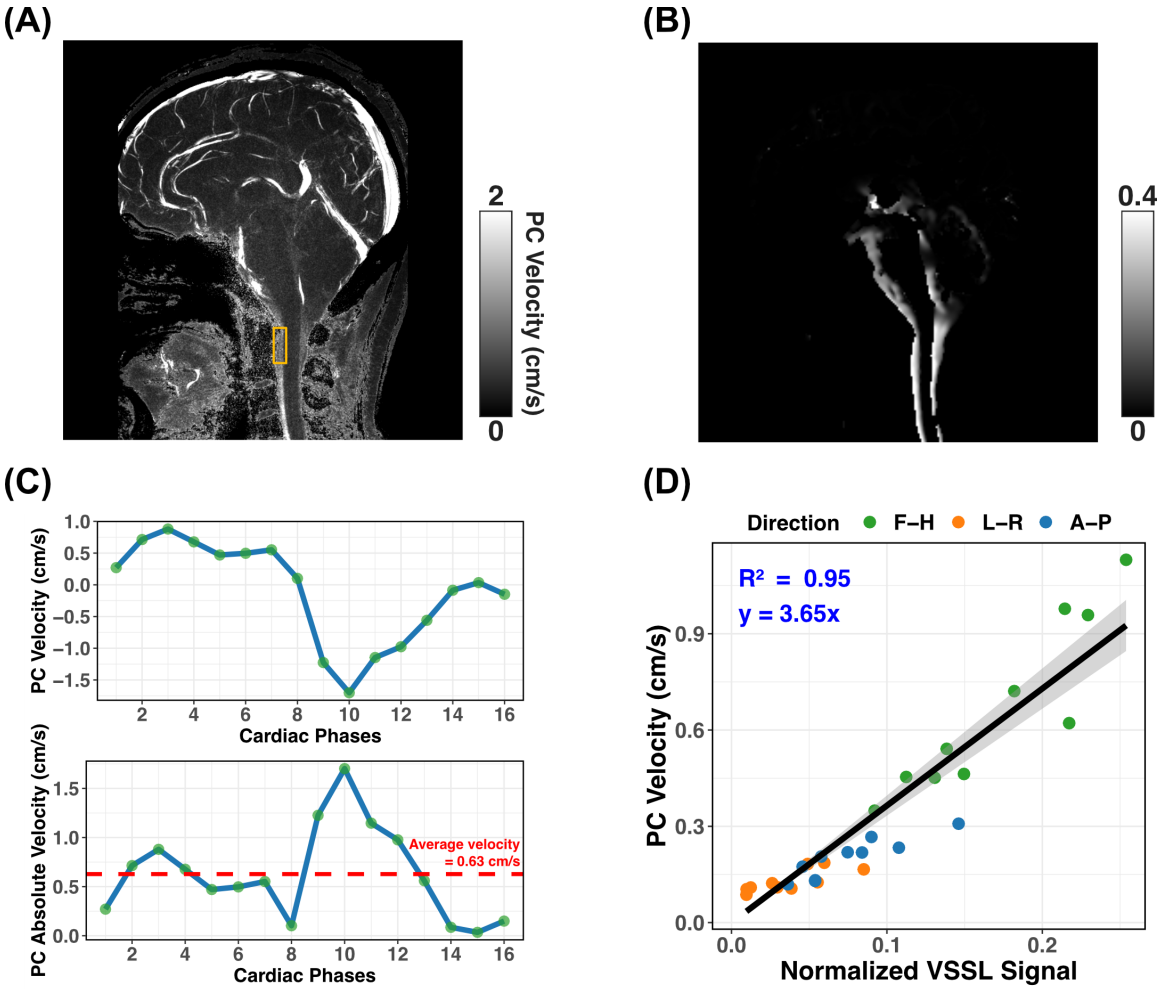

Figure 6. Calibration of VSSL with PC-MRI. (A) Velocity map obtained with PC-MRI for a representative healthy subject, showing pulsatile CSF flow throughout the SC, IPC, and blood flow in vessels. (B) Typical normalized VSSL images acquired with the S-I velocity-encoding direction on the same subject. (C) Representative PC flow curves with the S-I velocity-encoding direction for one cardiac cycle measured with pulse gating from the ROI shown in Figure A (yellow box). The procedure for calculating the average flow rate is illustrated in the image below. This involves taking the absolute values of the dynamic flow rates over cardiac cycle and then computing their average to obtain the final result. (D) Linear regression model between normalized VSSL signal and average velocity of the whole cardiac cycle in all three directions for the manually selected ROIs in the IPC, PPC, and SC. $R^2 = 0.95$.

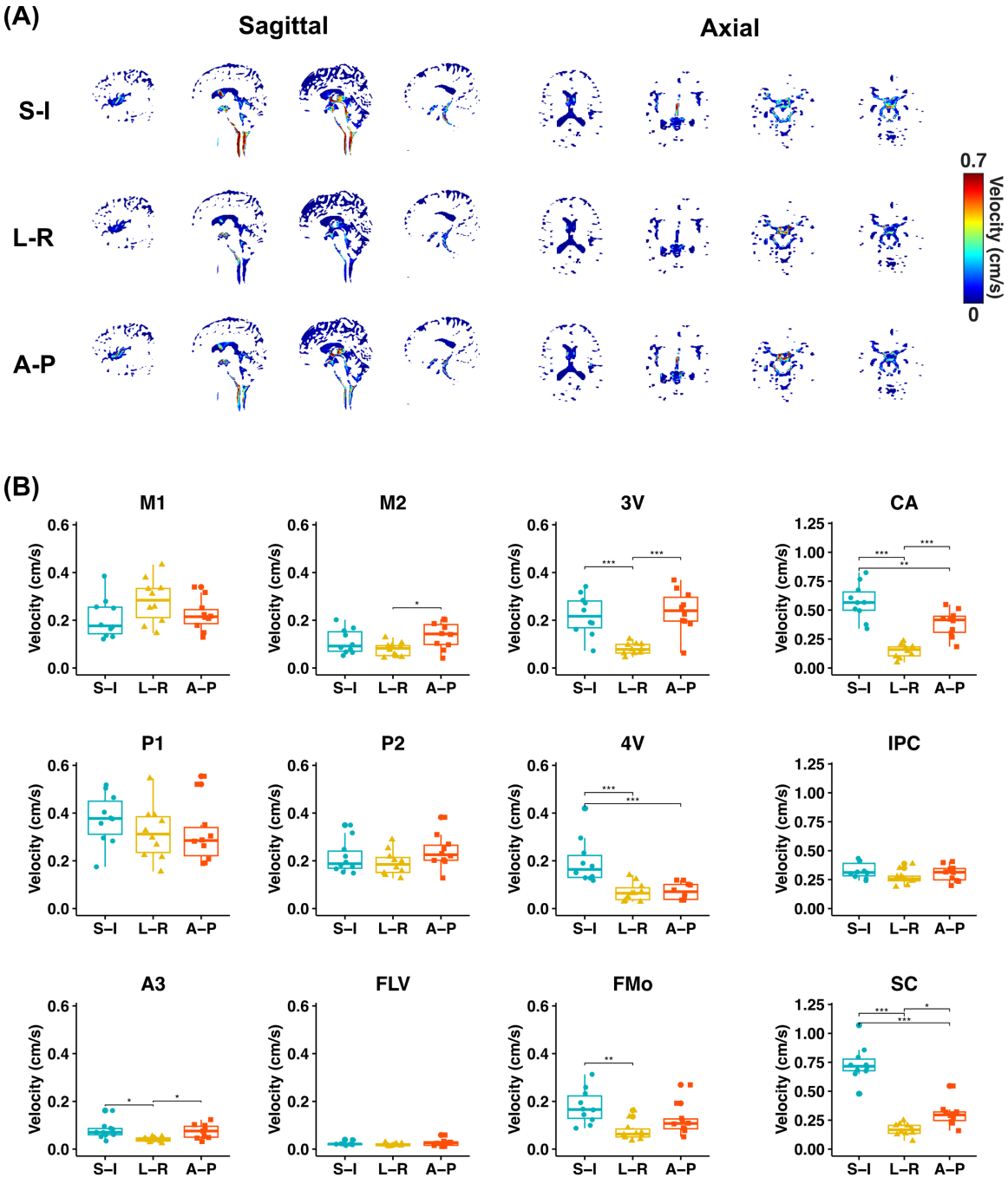

Figure 7. The VSSL-derived velocity maps for three different velocity-encoding directions. (A) The VSSL-derived velocity maps of S-I, A-P, and L-R directions for a representative healthy subject. (B) The boxplots of VSSL-derived velocity in each ROI across three orthogonal velocity-encoding directions. One-way ANOVA with post-hoc Tukey's honestly significant difference tests for pairwise comparisons was used for comparison (* $p < 0.05$, ** $p < 0.01$, *** $p < 0.001$).

Figure S1. Simulated Mz-velocity responses for the VSSL pulse train with segment times (T_{seg}) as 10 (A), 20 (B), 30 (C), 40 (D), and 50 (E) ms. Velocity-sensitive and velocity-compensated profiles are represented by solid and dashed blue lines, respectively. The cut-off velocity (V_{cut}) is delineated at the first intersection where $\Delta M = 1$, highlighted by vertical black dashed lines. Parameters used in the simulation, such as number of segments (8) and G_{max} (40 mT/m), are consistent with those employed in our study.

Figure S2. The VSSL images (top row) and M0 images (bottom row) with different TEs (TE = 816 and 39 ms).

Figure S3. The cross-sections of the M1 (A), M2 (B), P1 (C), and P2 (D) arteries. The blood vessels are shown in red, and the VSSL signal is displayed in green. Insert images show the magnified views of the PVSAS around arteries.